

# **OPEN**

# Insights into the role of CuO in the CO<sub>2</sub> photoreduction process

André E. Nogueira<sup>1,2</sup>, Jéssica A. Oliveira<sup>2,3</sup>, Gelson T. S. T. da Silva<sup>2,4</sup> & Caue Ribeiro <sup>0,2,5</sup>

The CO<sub>2</sub> photoreduction process to produce light hydrocarbons is known to be influenced by the presence of CuO nanoparticles, but the actual role of this material, whether as a catalyst or a reactant, has not yet been revealed. In this work, we investigate the role of CuO nanoparticles produced by a solvothermal method as a catalyst in CO<sub>2</sub>-saturated water reaction media under UV light, considering the effects of different electrolytes (Na<sub>2</sub>C<sub>2</sub>O<sub>4</sub>, KBrO<sub>3</sub>, and NaOH) and temperatures on nanoparticle phase and activity. The electrolyte strongly influenced product selectivity (NaOH led to evolution of CH<sub>4</sub>, Na<sub>2</sub>C<sub>2</sub>O<sub>4</sub> to CO, and KBrO<sub>3</sub> to O<sub>2</sub>) and induced CuO phase change. A long-term analysis of these processes indicated that during the initial steps, CuO acted as a reactant, rather than as a catalyst, and was converted to CuCO<sub>3</sub>.Cu(OH)<sub>2</sub>, while the as-converted material acted as a catalyst in CO<sub>2</sub> photoreduction, with conversion values comparable to those reported in the literature.

The increase in use of fossil fuels for energy production raises serious concerns from the environmental point of view. Allied to this energy demand, the emission of carbon dioxide ( $CO_2$ ), the most significant gas related to the greenhouse effect, contributes significantly to climate change, requiring new strategic approaches and control of emissions<sup>1,2</sup>. In order to contribute to achieving sustainable sources of energy, photocatalytic materials have been developed for the conversion of  $CO_2$  to useful chemical compounds and fuels, employing solar ultraviolet (UV) and visible radiation in a so-called artificial photosynthesis process<sup>3–5</sup>.

In heterogeneous photocatalysis, when semiconductors are illuminated with energy equal to or greater than the energy of the band gap, electron transfer from the valence band (VB) to the conduction band (CB) generates electron/hole pairs, providing reductive and oxidative sites, respectively $^6$ . Photogenerated electrons in the conduction band can then react with molecules adsorbed on the material surface, such as  $\rm CO_2$ , which is reduced to carbon monoxide, methane, ethanol, formic acid, and other added-value chemicals $^{2,6-8}$ .

Understanding of the various stages of the process is fundamental for the development of materials with appropriate characteristics for this application, as well as to improve the reaction conditions by the elimination of interferents and the addition of species able to enhance the photoreduction efficiency. However, although high  $\mathrm{CO}_2$  conversion values have been reported in the literature, the roles of different materials in this reaction were not revealed and there is no consensus concerning the most suitable material for catalysis of this reaction. The most studied semiconductor for this application is  $\mathrm{TiO}_2$ , however its low absorption in the visible region makes difficult the use of solar radiation in this process. Thus, a semiconductor that has been showing good results is copper oxide, but uncertainty remains about its actual role in the  $\mathrm{CO}_2$  photoreduction, whether as a catalyst or as a reactant  $^{9-12}$ . In addition, it is necessary to propose feasible photoreduction mechanisms and to determine the ways in which the most important reactive species influence product selectivity. To this end, evaluation of the effect of addition of electrolytes that act as radical, electron, or hole scavengers can clarify their roles in  $\mathrm{CO}_2$  photoreduction  $^{13-15}$ .

In this work, we systematically investigate  $CO_2$  photoreduction on CuO nanoparticles synthesized by a solvothermal method, employing different electrolytes and temperatures. The results revealed that CuO acted as a reactant, while as-formed copper carbonate could act as a catalyst in this reaction. The electrolytes influenced CuO phase change and product selectivity, helping to elucidate the ways in which the  $CO_2$  photoreduction process was assisted by this material.

<sup>1</sup>Brazilian Nanotechnology National Laboratory (LNNano), Brazilian Center for Research in Energy and Materials (CNPEM), Zip Code 13083-970, Campinas, São Paulo, Brazil. <sup>2</sup>Embrapa Instrumentation, Rua XV de Novembro, 1452, CEP: 13560-970, CP 741, São Carlos, SP, Brazil. <sup>3</sup>Department of Chemical Engineering, Federal University of São Carlos, Via Washington Luiz, km 235, CEP: 13565-905, São Carlos, SP, Brazil. <sup>4</sup>Department of Chemistry, Federal University of São Carlos, Via Washington Luiz, km 235, CEP: 13565-905, São Carlos, SP, Brazil. <sup>5</sup>Forschungszentrum Jülich GmbH, Institut für Energie- und Klimaforschung IEK-3 Elektrochemische Verfahrenstechnik, 52425, Jülich, Germany. Correspondence and requests for materials should be addressed to C.R. (email: caue.ribeiro@embrapa.br)

Received: 3 July 2018

Accepted: 26 November 2018

Published online: 04 February 2019

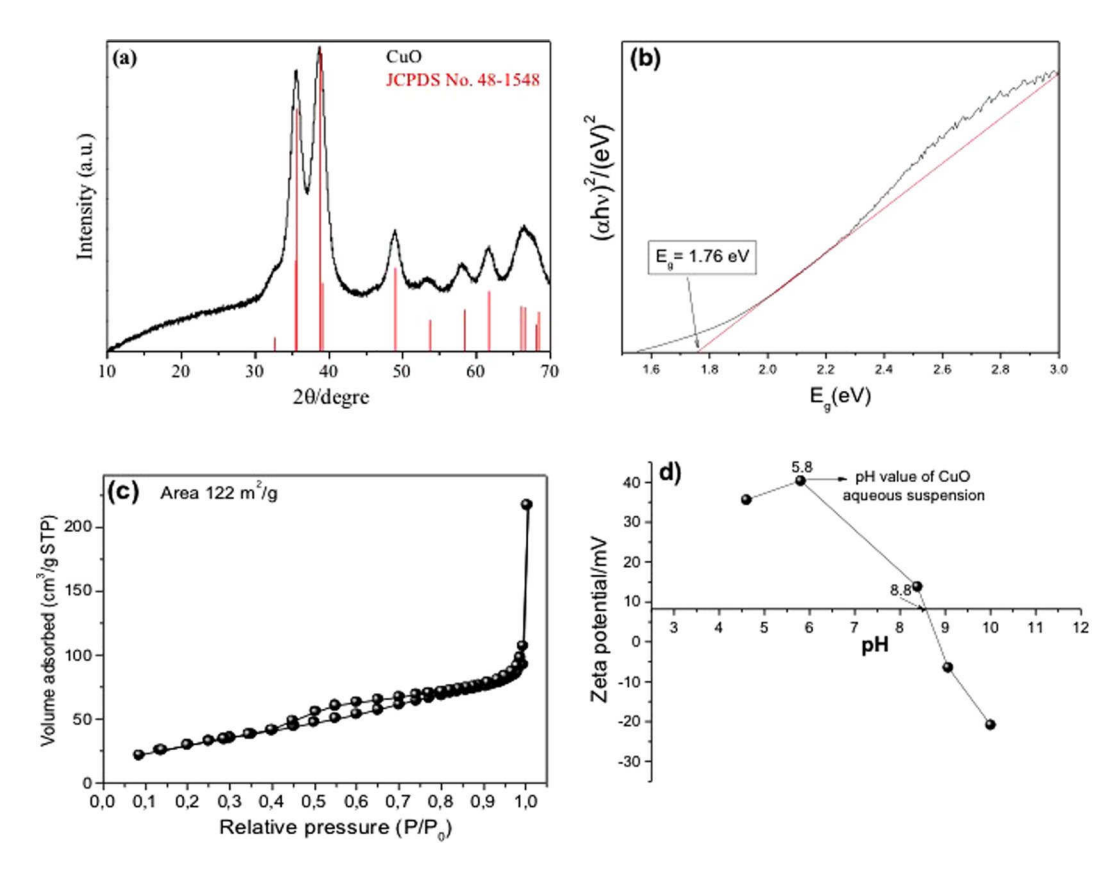


**Figure 1.** Analysis of the CuO: (a) XRD patterns, (b) UV-Vis diffuse reflectance spectra, (c) BET adsorption isotherm, and (d) zeta potential.

### **Results and Discussion**

**Characterization.** The XRD diffraction pattern of the CuO is shown in Fig. 1a. All the diffraction peaks could be indexed to a monoclinic structure (JCPDS 48–1548) and no impurities (such as  $Cu(OAc)_2$ ) were observed 16. The optical characteristics of the CuO were determined by UV-visible diffuse reflectance spectroscopy (Fig. 1b). The band gaps of the CuO were determined by fitting the optical transition at the absorption edges using the Tauc model, assuming that CuO has an indirect-type transition 17. The band gap value was obtained from the x-intecept of the tangent line for a plot of  $(\alpha h \nu)^2$  against energy  $(h\nu)$ , the measured band gap value was  $1.76 \, \text{eV}^{18-21}$ .

The porosity property of the CuO was investigated by  $N_2$  adsorption-desorption method (Fig. 1c). From this isotherm, it is observed that synthesized CuO nanoparticles exhibited type IV isotherm and the specific surface area was calculated by Brunauer, Emmett, and Teller (BET) method and the obtained value was  $122\,\mathrm{m}^2\,\mathrm{g}^{-1\,22}$ . Zeta potential analysis was performed to determine the CuO surface charge characteristics as a function of pH, since pH exerted a strong influence on the interaction between CO<sub>2</sub> and the CuO surface. Figure 1d shows the CuO zeta potential plotted as a function of pH, with a predominantly positive charge density in an aqueous medium. The suspension was at pH 6.0 without any electrolyte, and the isoelectric point of the CuO was at pH  $\approx$  8.8.

The morphology of the CuO was analyzed by FESEM and HRTEM. The FESEM image (Fig. 2) revealed that the nanoparticles presented a homogeneous coral-like architecture composed of aggregates of CuO nanospheres. The HRTEM measurements (Fig. 2e) confirmed that synthesis of the CuO nanoparticles by the solvothermal method resulted in the formation of a monoclinic crystalline structure, in agreement with previous work of our group<sup>16</sup>.

**Photoreduction tests.** Effect of the electrolytes. Evaluation of the photocatalytic activity of the CuO for  $CO_2$  photoreduction in aqueous solutions of  $Na_2C_2O_4$ ,  $KBrO_3$ , and NaOH, as well as in pure water, was performed under UV irradiation (Fig. 3). Four blank condition tests were conducted in order to obtain baselines, with irradiation in the absence of the catalyst (see Supplementary Information).

Analysis of the gas samples indicated that only  $CH_4$  was formed when the  $CO_2$  photoreduction was carried out in water or in sodium hydroxide solution. Increasing formation of  $CH_4$  was observed during 24 h under continuous irradiation (Fig. 3a), and the results indicated that water was more effective than aqueous sodium hydroxide solution for the reduction of  $CO_2$  to  $CH_4$ . This was probably related to the isoelectric point of  $CO_2$  (Fig. 1d), which was at  $pH \approx 8.8$ . Considering that the NaOH solution had  $pH \approx 9-10$ , this indicated that the  $CO_2$  surface charge was negative under this condition, with electron migration to the surface being less probable and  $CO_2$  adsorption not being favored. This was because at higher pH, the solubility of  $CO_2$  increases (forming  $CO_3^{2-}$ ), hence influencing the adsorption process and interfering in the  $CO_2$  photoreduction<sup>23</sup>. However, the

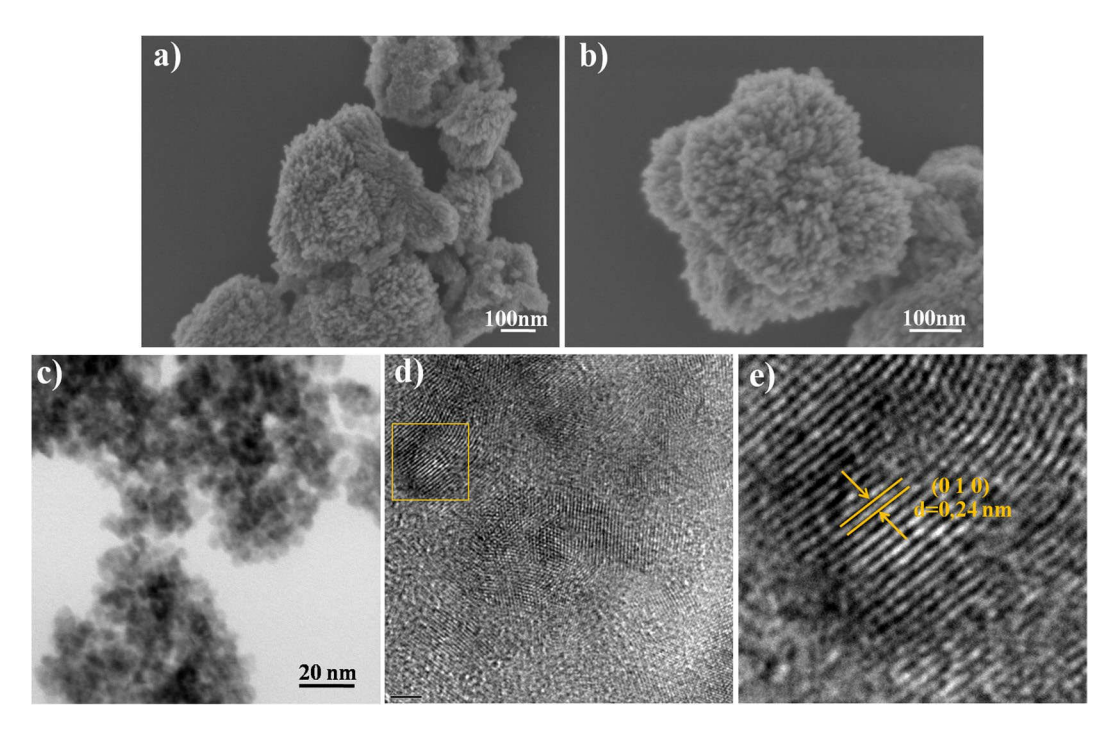


**Figure 2.** Electron microscopy analysis of CuO: (a,b) FESEM images; (c,d) low-magnification TEM images; (e) HRTEM image of selected area in (d).

specie prevailing in equilibrium in our system (using other electrolytes) is  $HCO_3^-$ , which was assumed to be the main reactant since all reactions occurred at pH ranging from 7 to 9 in non-saline medium (in this range, at least 80% of total dissolved carbon is  $HCO_3^-$ )<sup>24</sup>.

In the first step of the photocatalytic process,  $CO_2$  adsorbed on the CuO catalyst surface reacted with electrons to produce carbon dioxide radicals ( $CO_2^{\bullet-}$ ), which then reacted with H<sup>+</sup> to form surface CO and C, ultimately producing  $CH_4^{10,25}$ :

$$CO_2 \xrightarrow{e^-} CO_2^{\bullet-} \xrightarrow{H^+ + e^-} CO \xrightarrow{H^+ + 2e^-} C \xrightarrow{4H^+ + 4e^-} CH_4$$
 (1)

The importance of the participation of water splitting by the holes in the formation of certain products such as  $CH_4$  can be elucidated by the addition of species that inject electrons preferentially into the semiconductor. Sodium oxalate, for example, can be used  $^{26}$ , since it reacts directly with the holes, as represented by Equation 2, so  $H^+$  generation is suppressed, favoring only the CO formation reaction (Equation 3) (Fig. 4b) $^{27,28}$ . However, when the reaction was carried out in aqueous  $KBrO_3$  solution, only  $O_2$  was detected, as shown in Fig. 3c. Sodium oxalate is consumed in the reaction that generates electrons, as shown in Equations 2 and 3.

$$(COONa)_2 + 2h^+ \rightarrow 2CO_{2(g)} + 2Na^+_{(aq)}$$
 (2)

$$CO_2^{\bullet -} + 2CO_2 \to CO + CO_3^{2-}$$
 (3)

In the case of  $O_2$  evolution,  $BrO_3^-$  acts as an electron scavenger, hence suppressing any  $CO_2$  reduction. It is therefore expected that this compound will be reduced in the same way, forming  $Br^-$ . The participation of electrons in the photoreduction process was related to the ability to reduce the  $CO_2$  present in the reaction medium to the  $CO_2^{\bullet-}$  radical<sup>29</sup>. The addition of  $KBrO_3$  at low concentrations impaired formation of the  $CO_2^{\bullet-}$  radical, due to its high capacity to capture electrons. On the other hand, it hindered recombination by generating more holes for the reaction with water molecules, hence damaging the photoreduction process (Fig. 4c).

It can be seen in Fig. 5 that the amount of  $CO_2$  present in the headspace remained practically constant throughout the reaction (24 hours). The small oscillations observed are attributed to the displacement caused by the system in search of a chemical equilibrium between the  $CO_2$  dissolved in the liquid phase and that in the gas phase. The  $CO_2$  dissolved is consumed during the photoreaction reaction and to maintain the  $CO_2$  saturated medium, the gaseous  $CO_2$  moves into the liquid. It is worth mentioning that the long-term  $CO_2$  level was around  $149-151\,\mu\text{mol.L}^{-1}.g^{-1}$  for all samples, indicating that despite the small variation observed,  $CO_2$  concentration could be considered constant over long periods of reaction.

Effect of temperature. Figure 6 shows the temperature dependence of the photoreduction of  $CO_2$  to  $CH_4$  in pure water, from which it can be seen that there was an optimum temperature for the process. This could be due to lower  $CO_2$  saturation (see Supplementary Material: Table S1)<sup>30</sup>. Therefore, very high temperatures could

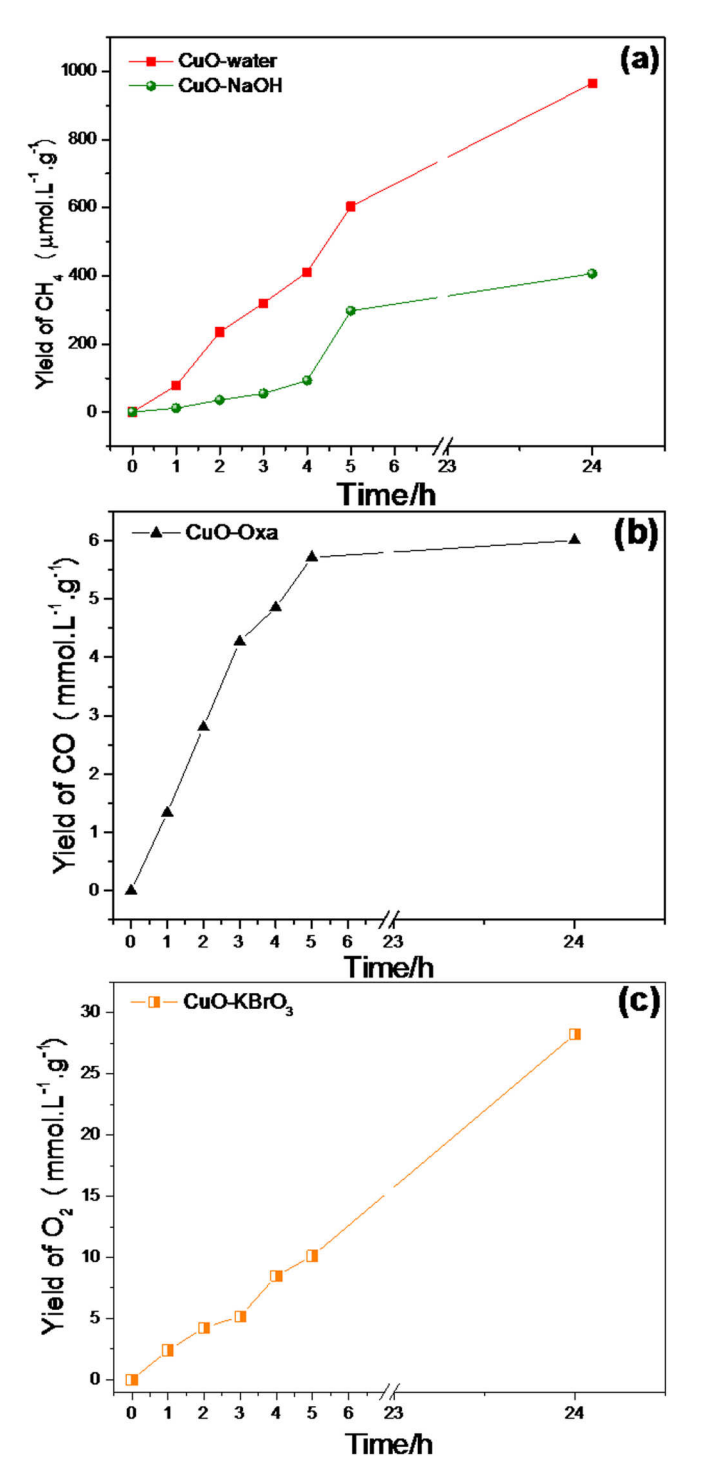


**Figure 3.** Products distribution for the photocatalytic reduction of CO<sub>2</sub> with (**a**) H<sub>2</sub>O and NaOH, (**b**) sodium oxalate, and (**c**) KBrO<sub>3</sub>.

negatively affect the reaction rate, due to the shift of  $CO_2$  saturation towards lower values<sup>31</sup>. It can be seen from Fig. 6 that the best temperature for the photoreduction of  $CO_2$  to  $CH_4$  was around  $25\pm3\,^{\circ}C$ . The activity was measured by the  $CH_4$  yields (Equation 4) and rates (Equation 5):

$$y_{CH_4} = \frac{n_{CH_2}}{V. m_{cat}} \tag{4}$$

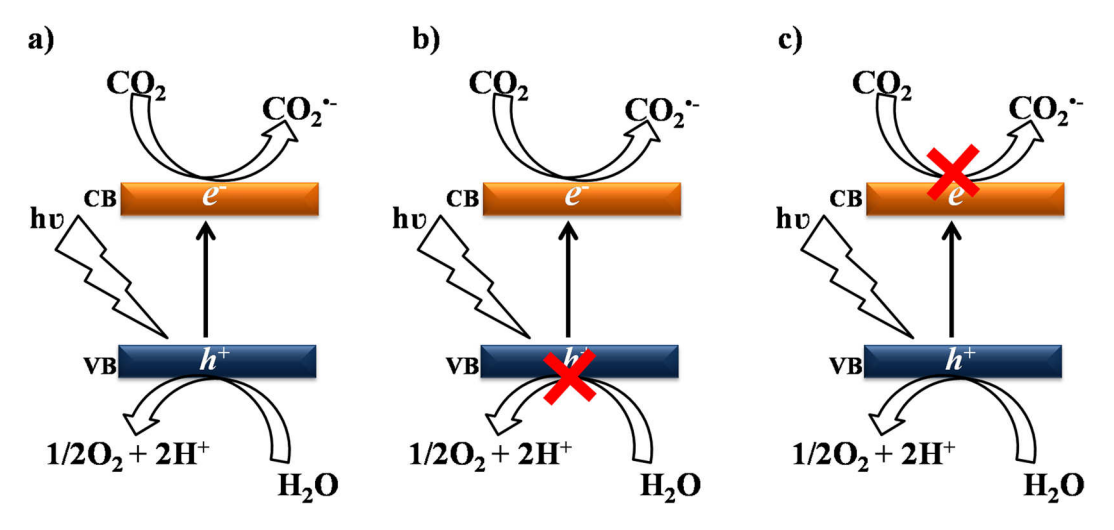


**Figure 4.** Schematic representation of the effect of the electrolyte in the photoreduction process: (a) pure water and NaOH, (b) sodium oxalate, and (c) KBrO<sub>3</sub>.

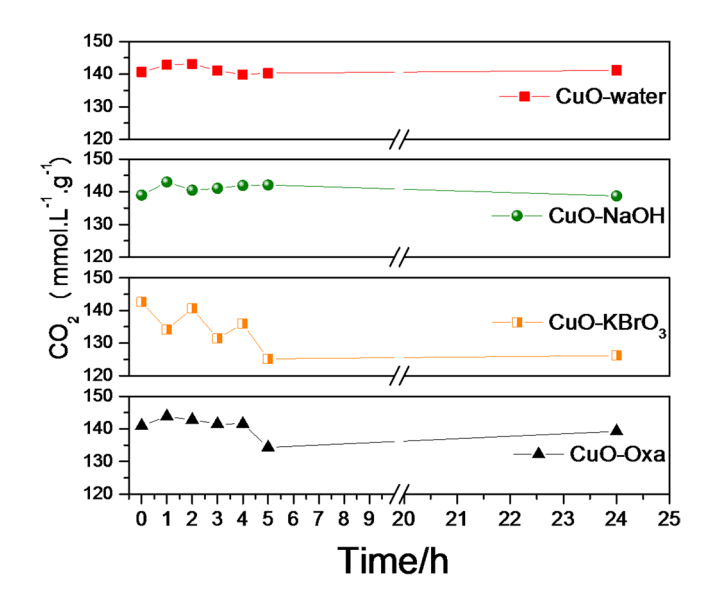


Figure 5. Concentration of CO<sub>2</sub> as a function of UV irradiation time.

$$R_{CH_4} = \frac{n_{CH_4}}{t[V. \ m_{cat}]} \tag{5}$$

The production rates of  $CH_4$  in 5 h of reaction at different temperatures are shown in Table 1. The reaction conducted at temperature of 25 °C showed the highest rate of approximately 121  $\mu$ mol/L.g<sub>cat</sub>.h, being 13 higher than the reaction conducted at 80 °C.

The reutilization of CuO in the  $CO_2$  photoreduction process was evaluated in four successive runs, while keeping the experimental conditions unchanged. As shown in Fig. 7, there was a high decrease (to  $\approx$ 78%) after the first photoreduction cycle, due to the conversion of CuO to copper carbonate, while the  $CO_2$  photoreduction became stabilized after three cycles.

All the reduction experiments (Fig. 3) showed saturation profiles, which was probably due to saturation of the headspace and consumption of the  $\rm CO_2$  available for reaction (since all the experiments were performed in batch mode). However, this profile could also be related to catalyst poisoning, or to the consumption or transformation of  $\rm CuO$  during the experiment (with the  $\rm CuO$  acting as a reactant, rather than purely as a catalyst). In order to elucidate these possible paths, the material was characterized after the reduction reaction under each tested condition.

The XRD patterns revealed noticeable changes in the structures of the materials after the reactions (Fig. 8). In the reaction using sodium oxalate solution, the material presented  $2\theta$  peaks at 43.5° and 50.5°, corresponding to planes (111) and (200), respectively, related to metallic copper (JCPDS 04-0836), together with peaks centered at

Temperature (°C)	Yield (μmol/L.g <sub>cat</sub> )	Rate (µmol/L. g <sub>cat</sub> .h <sup>-1</sup> )
10	299	59.8
25	606	121.2
50	110	22.0
80	44	8.8

**Table 1.** Yields and Rate constants for the  $CO_2$  photoreduction reaction catalyzed by CuO at different temperatures under UV irradiation after 5 h of reaction.

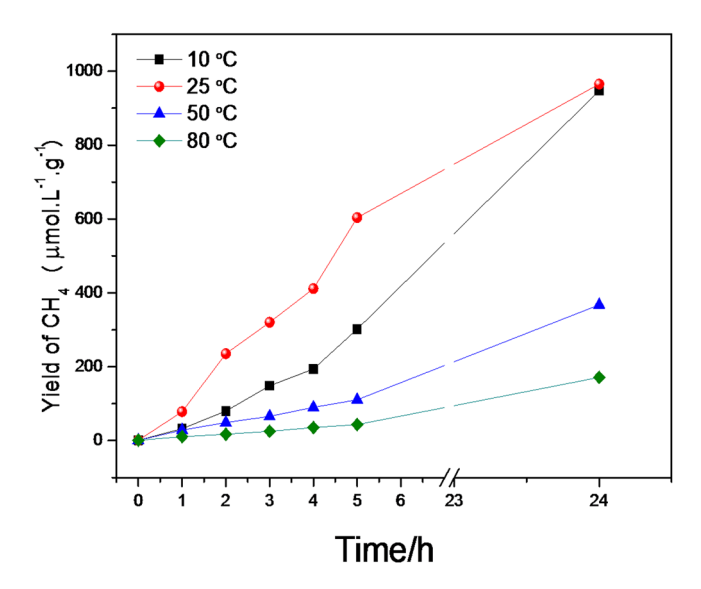


**Figure 6.** Kinetics of CO<sub>2</sub> photoreduction at different temperatures.

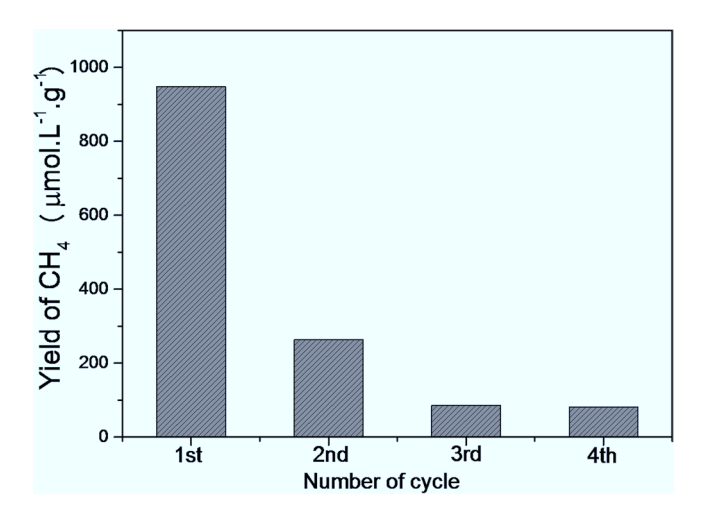


**Figure 7.** Activity of CuO after 24 h in successive cycles of the photocatalytic reduction of  $CO_2$  in  $H_2O$  at  $25 \pm 3$  °C.

 $2\theta$  of 36.5° and 61.0°, related to Cu<sub>2</sub>O, showing that after 24h the material had undergone a reduction process. On the other hand, when the reaction was performed using KBrO<sub>3</sub> or NaOH solutions, or pure water, the materials showed diffraction peaks related to copper carbonate (malachite, CuCO<sub>3</sub>.Cu(OH)<sub>2</sub>) (JCPDS 01-0959). In fact, the first evidence of reaction of CO<sub>2</sub> with CuO was a color change from brown to light green, indicative of copper carbonate formation<sup>32,33</sup>:

$$2Cu_{(s)} + H_2O_{(l)} + CO_{2(g)} + O_{2(g)} \rightarrow Cu(OH)_{2(s)} + CuCO_{3(s)}$$
 (6)

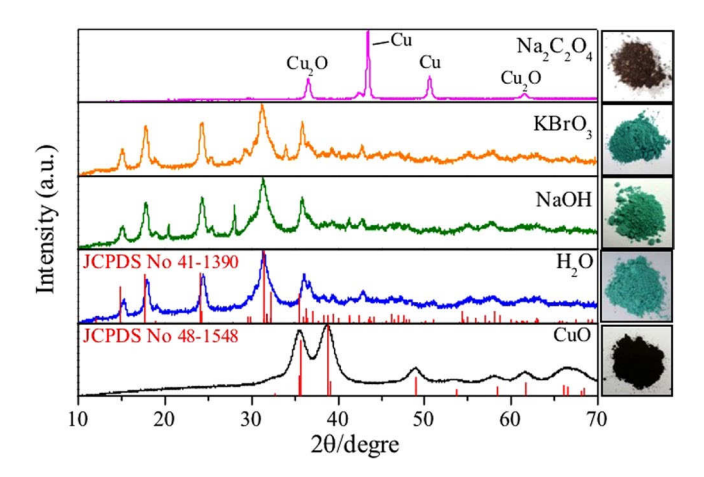


**Figure 8.** XRD patterns of catalysts before (CuO) and after reaction for 24 h under different conditions at  $25 \pm 3$  °C.

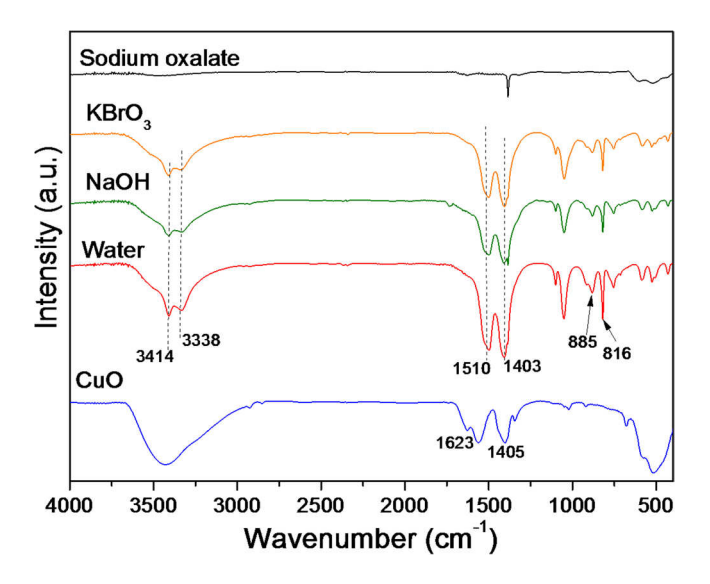


**Figure 9.** FTIR spectra of the materials after CO<sub>2</sub> photoreduction.

The FTIR spectra of the CuO surface before and after UV irradiation for 24 h are shown in Fig. 9. The FTIR spectrum of the as-prepared CuO showed a broad band at approximately 400–600 cm<sup>-1</sup>, attributed to the vibrations of Cu-O, and bands at 1623 and 1405 cm<sup>-1</sup>, related to asymmetric stretching of C-O and asymmetric bending of CH<sub>3</sub> of the copper acetate precursor, respectively<sup>23</sup>. After the CO<sub>2</sub> photoreduction using different electrolytes the FTIR spectra showed a different profile of the CuO sample before the reaction. Bands at 1510 cm<sup>-1</sup> and 1403 cm<sup>-1</sup> were related to C-O stretching modes, while those at 885 and 816 cm<sup>-1</sup> were due to C-O bending vibration modes. Bands at 3414 and 3338 cm<sup>-1</sup> could be attributed to O-H stretching modes, reflecting the presence of two different OH groups in the copper carbonate crystal lattice<sup>34-36</sup>.

FESEM and HRTEM was employed to examine morphological features of the materials after the photoreduction process (Figs 10 and 11). It was observed that not only did the CuO structure change, but the morphology also altered. The reactions performed in the presence of pure water and aqueous solutions of NaOH or KBrO $_3$  led to the formation of nanorods, while the reaction carried out in the presence of aqueous sodium oxalate solution led to the formation of metallic copper plates.

The findings were supported by comparison with conversion levels reported in the literature (Table 2). Considering studies with copper oxide and CuO-related materials, stable CO<sub>2</sub> conversions catalyzed by malachite were within the same range, suggesting that the same phenomenon was probably being observed (despite the fact that in all the earlier studies it was stated that the actual catalyst present was copper oxide).

From these results, we propose that the actual catalyst for  $CO_2$  reduction was the as-formed malachite phase, acting by surface adsorption and possible structural exchange.  $CO_2$  could be bonded to the surface of the material in three different ways, as monodentate carbonate, bidentate carbonate, and bidentate bicarbonate, as shown in Fig. 12  $^4$ . Under UV irradiation, the species adsorbed on the material surface could be easily transformed to  $CO_2^{\bullet-}$ , which is a key intermediate in  $CO_2$  photoreduction.

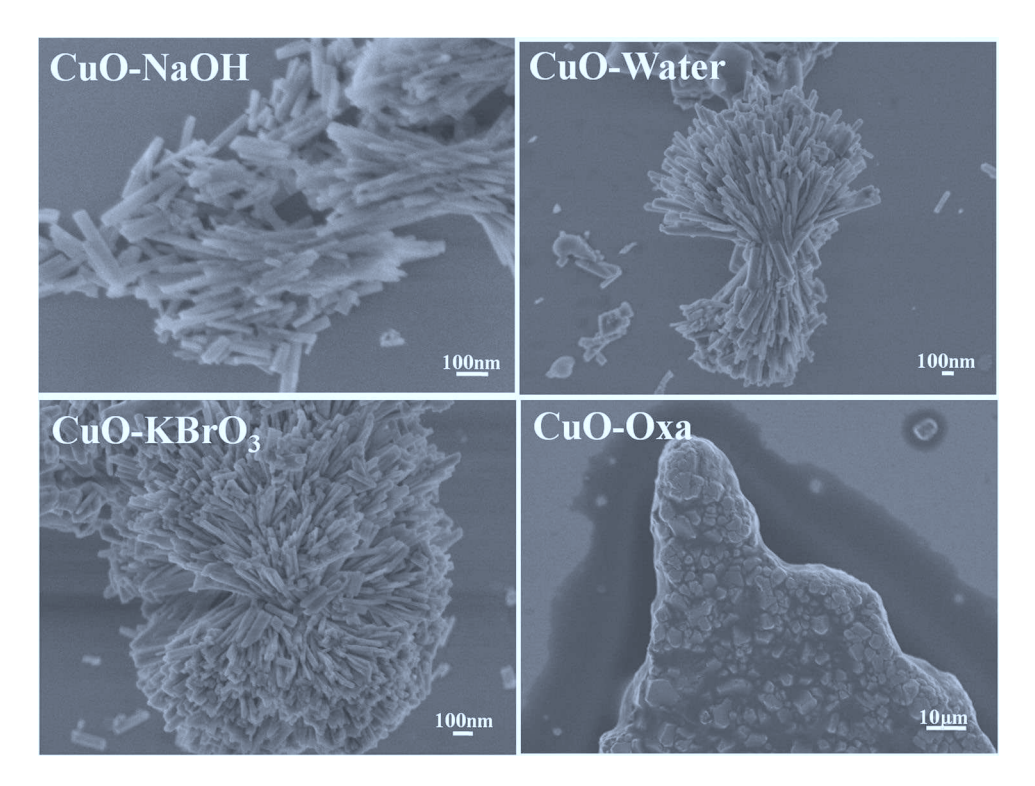


Figure 10. FESEM images of the materials after 24 h of reaction.

### Methods

**Solvothermal synthesis of CuO.** The CuO nanoparticles were synthesized by adding  $50\,\mathrm{mL}$  of a  $0.05\,\mathrm{M}$  solution of copper acetate in ethanol (99.5%, Synth) to a  $100\,\mathrm{mL}$  poly(tetrachlorethylene) capsule and then placing the capsule in an autoclave, under constant magnetic stirring<sup>37</sup>. The solvothermal treatment was performed at  $110\,^{\circ}\mathrm{C}$  for  $20\,\mathrm{h}$ . After the reaction, the autoclave was cooled naturally to room temperature. The product was recovered by centrifugation, washed two times in ethanol, and then dried in air at  $60\,^{\circ}\mathrm{C}$  for  $4\,\mathrm{h}$ .

**Characterization.** The CuO powder was characterized by X-ray diffraction (XRD), using CuK $\alpha$  radiation with  $\lambda = 0.15406$  nm, employing a Shimadzu XRD 6000 diffractometer operated at 30 mA and 30 kV, in the 20 range from 20 to 80°, with a scan step of 0.02°. The morphologies of the materials were characterized by high resolution transmission electron microscopy (HRTEM), using a TECNAI G2 F20 microscope (FEI) operated at 200 kV, and by field emission scanning electron microscopy (FESEM), using a JSM 6701 F microscope (JEOL) operated at 5 kV. The HRTEM samples were prepared by wetting carbon-coated copper grids with a drop of the colloidal suspensions and then drying in air.

The specific surface areas of the materials were measured using nitrogen adsorption at 77 K (ASAP-2020, Micromeritics), with calculation according to the Brunauer-Emmett-Teller (BET) method. Prior to the analyses, the samples were pre-treated (degassed) by heating at 70 °C under vacuum until reaching a pressure of less than 20 mm Hg. Diffuse reflectance spectra (DRS) in the ultraviolet-visible region were recorded between 200 and 800 nm, at room temperature, using a Cary 5 G instrument (Varian) operated in diffuse reflectance mode. The band gaps of the samples were determined according to the method proposed by Tauc $^{38,39}$ . Infrared (FTIR) spectra of the materials were obtained in the range from 4000 to  $400\,\mathrm{cm}^{-1}$ , with 32 scans and  $4\,\mathrm{cm}^{-1}$  resolution, using a Spectrum 1000 spectrophotometer (Perkin Elmer). The zeta potentials of dilute suspensions of the materials were measured with a Zeta Sizer nano-ZS instrument (Malvern Instruments), in the pH range from 11 to 4, with the pH adjusted by adding 0.1 M HCl or 0.1 M NaOH.

 ${
m CO_2}$  photoreduction. The  ${
m CO_2}$  photoreduction was performed in a 500 mL capacity cylindrical acrylic reactor, covered with borosilicate glass. A 0.3 g quantity of the catalyst was suspended in 300 mL of solutions of NaOH (0.1 M), Na<sub>2</sub>C<sub>2</sub>O<sub>4</sub> (0.1 M), or KBrO<sub>3</sub> (0.1 M), or in pure water. Ultrapure  ${
m CO_2}$  was bubbled through the reactor for at least 20 min to ensure that all the dissolved oxygen was eliminated. The illumination system employed a 5 W UVC lamp (Philips) with a wavelength of 253.7 nm, positioned in the center of the reactor. The measured intensity of the incident light was 5.5 mW cm<sup>-2</sup>. A detailed description of the photoreactor system is provided in the Supplementary Information.

The progress of the reaction was monitored by collecting and analyzing samples at regular intervals. Gaseous products were determined by GC-TCD and GC-FID (model CP-3800 gas chromatograph, Varian), using a packed column (HayeSep N,  $0.5 \, \text{m} \times 1/8''$ ). The gas flow rates were  $30 \, \text{mL} \, \text{min}^{-1}$  (H<sub>2</sub>),  $300 \, \text{mL} \, \text{min}^{-1}$  (air), and  $30 \, \text{mL} \, \text{min}^{-1}$  (N<sub>2</sub>). The injector, TCD, and FID temperatures were 150, 200, and 150 °C, respectively. The sample injection volume was  $2 \, \mu \text{L}$ , and the yield was calculated using injections of standard gaseous mixtures.

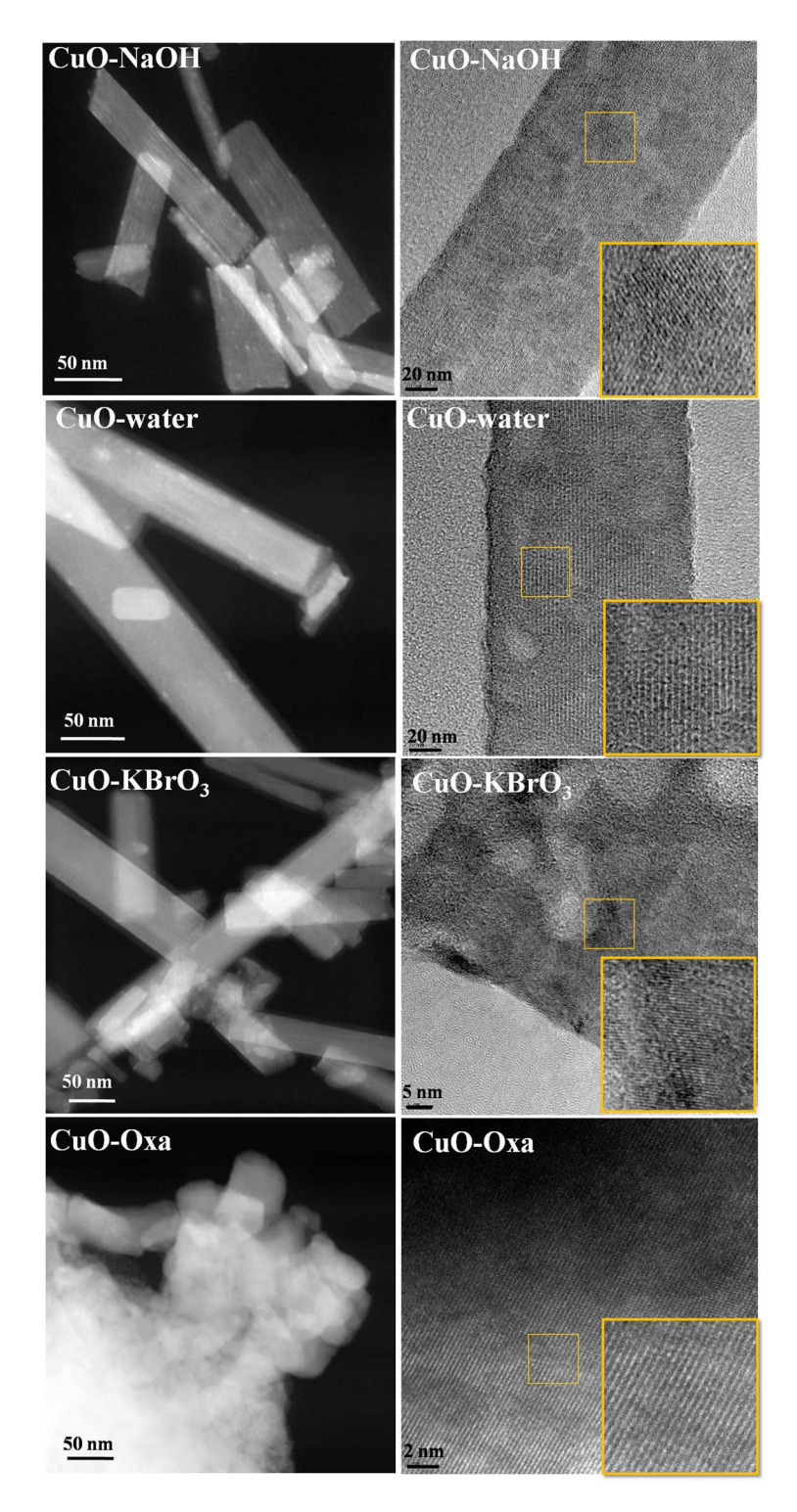


Figure 11. HRTEM images of the materials after 24h of reaction.

Blank reactions were carried out to ensure that the  $\mathrm{CH_4}$  and  $\mathrm{CO}$  originated from the photoreduction of  $\mathrm{CO_2}$  see Supplementary Information. In the first blank reactions, no catalyst was added, and all other conditions were maintained the same, in the second test the reaction was conducted in nitrogen atmosphere.

# Conclusion

Concluding, we observed that CuO was not stable during the  $CO_2$  photoreduction process, with CuO changing to malachite (CuCO<sub>3</sub>·Cu(OH)<sub>2</sub>). However, significant  $CO_2$  conversion was observed during the CuO carbonation process, and the performance of malachite as a catalyst was comparable to results reported in the literature, where the catalyst was assumed to be CuO. The nature of the electrolyte influenced product selectivity, with CuO phase

Figure 12. Schematic diagram of species adsorbed on the CuO surface in the CO<sub>2</sub> adsorption process.

Catalysts	Condition	Irradiance	CH <sub>4</sub> (μmol.g <sup>-1</sup> h <sup>-1</sup> )	Ref.
CuO	300 W Xe lamp	100 mW cm <sup>-2</sup>	2.96	9*
CuO	100 W Xenon solar	_	19.7	10*
Cu <sub>2</sub> O	125 W Hg lamp	_	16.0	11
Cu <sub>2</sub> O/TiO <sub>2</sub>	300 W Xe lamp	20.5 mW cm <sup>-2</sup>	0.99	12
CuO	5 W UVC lamp	5.5 mW cm <sup>-2</sup>	39.5	This work

**Table 2.** CuO-based photocatalytic systems for CO<sub>2</sub> reduction to CH<sub>4</sub>. \*Normalized units.

change participating in the processes. The results reported here contribute to elucidation of the role of CuO in the  $\rm CO_2$  photoreduction process, providing important information for the rational development of Cu-based catalysts for this process.

# References

- 1. Das, S. & Daud, W. A review on advances in photocatalysts towards CO2 conversion. RSC Advances 4, 20856-20893 (2014).
- 2. Zhou, R. & Guzman, M. I. CO<sub>2</sub> Reduction under Periodic Illumination of ZnS J. Phys. Chem. C 118, 11649-11656 (2014).
- 3. Liu, L. & Li, Y. Understanding the Reaction Mechanism of Photocatalytic Reduction of CO<sub>2</sub> with H<sub>2</sub>O on TiO<sub>2</sub> -Based Photocatalysts: A Review Aerosol. *Air Qual. Res.* **2**, 453–469 (2014).
- Wang, Y. et al. CO<sub>2</sub> photoreduction with H<sub>2</sub>O vapor on highly dispersed CeO<sub>2</sub>/TiO<sub>2</sub> catalysts: Surface species and their reactivity. J. Catal. 337, 293–302 (2016).
- Aguirre, M. E., Zhou, R., Eugene, A. J., Guzman, M. I. & Grela, M. A. Environmental Cu<sub>2</sub>O/TiO<sub>2</sub> heterostructures for CO<sub>2</sub> reduction through a direct Z-scheme: Protecting Cu<sub>2</sub>O from photocorrosion. Appl. Catal. B 217, 485–493 (2017).
- Fujishima, A., Inoue, T., Konishi, S. & Honda, K. Photoelectrocatalytic reduction of carbon dioxide in aqueous suspensions of semiconductor powders. *Nature* 277, 637–638 (1979).
- 7. Mao, J., Li, K. & Peng, T. Recent advances in the photocatalytic CO<sub>2</sub> reduction over semiconductors. *Catal. Sci. and Tech.* **3**, 2481 (2013).
- 8. Zhou, R. & Guzman, M. I. Photocatalytic Reduction of Fumarate to Succinate on ZnS MineralSurfaces. J. Phis. Chem. C. 120, 7349–7357 (2016).
- 9. In, S. L., Vaughn, D. D. & Schaak, R. E. Hybrid CuO-TiO2 À x N x Hollow Nanocubes for Photocatalytic Conversion of CO2 into Methane under Solar Irradiation. *Angew. Chem.* **51**, 3915–3918 (2012).
- Park, S. et al. Hybrid Cu<sub>x</sub>O-TiO<sub>2</sub> Heterostructured Composites for Photocatalytic CO<sub>2</sub> Reduction into Methane Using Solar Irradiation. ACS Omega 1, 868–875 (2016).
- Ovcharov, M. L., Mishura, A. M., Shcherban, N. D., Filonenko, S. M. & Granchak, V. M. Photocatalytic reduction of CO<sub>2</sub> using nanostructured Cu<sub>2</sub>O with foam-like structure. Solar Energy 139, 452 (2016).
- 12. Zhuo, X. et al. Selective photocatalytic reduction of CO<sub>2</sub> into CH<sub>4</sub> over Pt-Cu<sub>2</sub>O TiO<sub>2</sub> nanocrystals: The interaction between Pt and Cu<sub>2</sub>O cocatalysts. Appl. Catal. B **202**, 695–703 (2017).
- 13. Li, Y., Wang, J., Yao, H., Dang, L. & Li, Z. Efficient decomposition of organic compounds and reaction mechanism with BiOI photocatalyst under visible light irradiation. *J. Mol. Catal. A, Chem.* 334, 116–122 (2011).
- Renaudde, R., Ming, T., Davies, P., Wei, L. & Sylvain, C. Removal of non-CO<sub>2</sub> greenhouse gases by large-scale atmospheric solar photocatalysis. *Prog. Energy Combust. Sci.* 60, 68–96 (2017).
- 15. Villa, K., Murcia-lópez, S., Andreu, T. & Ramón, J. Mesoporous WO<sub>3</sub> photocatalyst for the partial oxidation of methane to methanol using electron scavengers. *Appl. Catal. B* **163**, 150–155 (2015).
- Nogueira, A. E., Giroto, A. S., Neto, A. B. S. & Ribeiro, C. CuO synthesized by solvothermal method as a high capacity adsorbent for hexavalent chromium Colloids. Surfaces A Physicochem. Eng. Asp. 498, 161–167 (2016).
- Radhakrishnan, A. A. & Beena, B. B. Structural and Optical Absorption Analysis of CuO Nanoparticles. *Indian J. of Adv. Chem. Sci.* 2, 158–161 (2014).
- Roy, S. C., Varghese, O. K. & Paulose, M. Toward Solar Fuels: Photocatalytic Conversion of Carbon Dioxide to Hydrocarbons. ACS Nano. 4, 1259–1278 (2010).
- 19. Heinemann, M., Eifert, B. & Heiliger, C. Band structure and phase stability of the copper oxides Cu<sub>2</sub>O, CuO, and Cu<sub>4</sub>O<sub>3</sub>. *Phys. Rev. B Condens. Matter Mater. Phys.* 87, 3–7 (2013).
- Mallick, P. & Sahu, S. Structure, Microstructure and Optical Absorption Analysis of CuO Nanoparticles Synthesized by Sol-Gel Route. Nanosci. Nanotechnol. 2, 71–74 (2012).
- 21. Marabelli, F., Parravicini, G. B. & Salghetti-Drioli, F. Optical gap of CuO. Phys. Rev. B 52, 1433–1436 (1995).
- 22. Matthias, T. et al. Physisorption of gases, with special reference to the evaluation of surface area and pore size distribution (IUPAC Technical Report). Pure Appl. Chem. 87, 1051–1069 (2015).
- 23. Roldan, A. et al. Bio-inspired CO<sub>2</sub> conversion by iron sulfide catalysts under sustainable conditions. Chem. Commun. 51, 7501–7504 (2015).
- 24. Mook, W. Environmental Isotopes in the Hydrological Cycle: Principles and Applications, Chapter "Chemistry of carbonic acid in water" pp. 143–165, INEA/UNESCO: Paris (2000).
- 25. Kwak, B. S. & Kang, M. Photocatalytic reduction of CO<sub>2</sub> with H<sub>2</sub>O using perovskite Ca<sub>x</sub>Ti<sub>v</sub>O<sub>3</sub>. Appl. Surf. Sci. 337, 138–144 (2015).

- 26. Ju, P., Wang, Y., Sun, Y. & Zhang, D. Controllable one-pot synthesis of a nest-like Bi<sub>2</sub>WO<sub>6</sub>/BiVO<sub>4</sub> composite with enhanced photocatalytic antifouling performance under visible light irradiation. *Dalton Trans.* 45, 4588–4602 (2016).
- 27. Karamian, E. & Sharifnia, S. On the general mechanism of photocatalytic reduction of CO<sub>2</sub>. J. CO2 Util. 16, 194–203 (2016).
- 28. Yue, M., Wang, R., Cheng, N., Gao, W. & Yang, T. ZnCr<sub>2</sub>S<sub>4</sub>. Highly effective photocatalyst converting nitrate into N<sub>2</sub> without over-reduction under both UV and pure visible light. Sci. Rep. 6, 1–11 (2016).
- 29. Nikokavoura, A. & Trapalis, C. Alternative photocatalysts to TiO<sub>2</sub> for the photocatalytic reduction of CO<sub>2</sub>. Appl. Surf. Sci. 391, 149–174 (2017).
- Carroll, J. J., Slupsky, J. D. & Mather, A. E. The Solubility of Carbon Dioxide in Water at Low Pressure. J. Phys. Chem. Ref. Data 20, 1201–1209 (1991).
- 31. Fogler, S. H. Elements of Chemical Reaction Engineering. (Prentice Hall, 2016).
- 32. Xi, T., Hong, S. & Xia, F. Green synthesis of CuO nano fl akes from CuCO<sub>3</sub>·Cu(OH)<sub>2</sub> powder and H<sub>2</sub>O<sub>2</sub> aqueous solution. *Powder Technol.* 228, 128–130 (2012).
- Yu-Kai, L. et al. Efficient hydrogen production using Cu-based catalysts prepared via homogeneous precipitation. J. Mat. Chem. 19, 9186–9194 (2009).
- Stoilova, D., Koleva, V. & Vassileva, V. Spectrochim. Infrared study of some synthetic phases of malachite (Cu<sub>2</sub>(OH)<sub>2</sub>CO<sub>3</sub>)
   – hydrozincite (Zn<sub>5</sub>(OH)<sub>6</sub>(CO<sub>3</sub>)<sub>2</sub>) series. Acta A Mol. Biomol. Spectrosc. 58, 2051–2059 (2002).
- 35. Schmidt, M. & Lutz, H. D. Hydrogen Bonding in Basic Copper Salts: a Spectroscopic Study of Malachite, Cu<sub>2</sub>(OH)<sub>2</sub>CO<sub>3</sub>, and Brochantite, Cu<sub>4</sub>(OH)<sub>6</sub>SO<sub>4</sub>. Phys. Chem. Miner. **2**, 27–32 (1993).
- 36. Lutz, H. D. Structure and strength of hydrogen bonds in inorganic solids. J. Mol. Struct. 646, 227-236 (2003).
- 37. Nogueira, A. E., Lopes, O. F., Neto, A. B. S. & Ribeiro, C. Enhanced Cr(VI) photoreduction in aqueous solution using Nb<sub>2</sub>O<sub>5</sub>/CuO heterostructures under UV and visible irradiation. *Chem. Eng. J.* **312**, 220–227 (2017).
- 38. Tolvaj, L., Mitsui, K. & Varga, D. Validity limits of Kubelka Munk theory for DRIFT spectra of photodegraded solid wood. Wood Sci. Tech. 45, 135–146 (2011).
- 39. Wood, D. L. & Tauc, J. Weak Absorption Tails in Amorphous Semiconductors. Phisical Rev. 5 (1972).

## Acknowledgements

The authors are grateful to the Ministry of Science, Technology, and Innovation (through SisNANO Program – National System of Laboratories in Nanotechnology), the National Council for Scientific and Technological Development (CNPq, Brazil China Virtual Center in Nanotechnology Project and grant #402.287/2013-4), Coordination for the Improvement of Higher Education Personnel (CAPES, grants CAPES-Embrapa and CAPES-Humboldt, Finance Code 001), Sao Paulo Research Foundation (FAPESP #15/14330-8, #16/09746-3, #16/21515-7 and #14/09014-7), and Embrapa Rede AgroNano for their financial support. Caue Ribeiro also acknowledge Chinese Academy of Sciences (CAS) President's International Fellowship Initiative (PIFI) by financial support and Alexander von Humboldt Foundation Fellowship for Experienced Researchers (Finance Code 001 - CAPES Process 88881.145566/2017-1. We thank the Brazilian Nanotechnology Laboratory for Research in Energy and Materials (LNNano) and the Structural Characterization Laboratory (LCE) for technical support during the X-ray photoelectron spectroscopy (grant #13839) and transmission electron microscopy experiments, respectively.

### **Author Contributions**

A.E.N. and C.R. designed research; A.E.N., J.A.O. and G.T.S.T.S. conducted the experiment; A.E.N., J.A.O. and G.T.S.T.S. and C.R. wrote the paper. All authors reviewed the manuscript.

## **Additional Information**

Supplementary information accompanies this paper at https://doi.org/10.1038/s41598-018-36683-8.

**Competing Interests:** The authors declare no competing interests.

**Publisher's note:** Springer Nature remains neutral with regard to jurisdictional claims in published maps and institutional affiliations.

Open Access This article is licensed under a Creative Commons Attribution 4.0 International License, which permits use, sharing, adaptation, distribution and reproduction in any medium or format, as long as you give appropriate credit to the original author(s) and the source, provide a link to the Creative Commons license, and indicate if changes were made. The images or other third party material in this article are included in the article's Creative Commons license, unless indicated otherwise in a credit line to the material. If material is not included in the article's Creative Commons license and your intended use is not permitted by statutory regulation or exceeds the permitted use, you will need to obtain permission directly from the copyright holder. To view a copy of this license, visit <a href="https://creativecommons.org/licenses/by/4.0/">https://creativecommons.org/licenses/by/4.0/</a>.

© The Author(s) 2019